Numerical Field Simulation for Parallel Transmission in MRI at 7 Tesla

by

Jessica A. Bernier

B.S. Physics, B.S. Mathematics
The University of Arizona, 2009

Submitted to the Department of Electrical Engineering and Computer Science
In Partial Fulfillment of the Requirements for the Degree of

MASTER OF SCIENCE IN ELECTRICAL ENGINEERING AND COMPUTER SCIENCE

at the

MASSACHUSETTS INSTITUTE OF TECHNOLOGY

JUNE 2011

Signature of author: _____
Department of Electrical Engineering and Computer Science
May 20, 2011

Certified by: _____
Jónas Adalsteinsson
Associate Professor of Electrical Engineering and Computer Science
Associate Professor of Harvard-MIT Health Sciences & Technology
Thesis Supervisor

Accepted by: _____
Leslie A. Kolodziejski
Professor of Electrical Engineering and Computer Science
Chairman, EECS committee of Graduate Students

Numerical Field Simulation for Parallel Transmission in MRI at 7 Tesla

by

Jessica A. Bernier

Submitted to the Department of Electrical Engineering and Computer Science

May 20, 2011

In Partial Fulfillment of the Requirements for the Degree of Master of Science in Electrical Engineering and Computer Science

ABSTRACT

Parallel transmission (pTx) is a promising improvement to coil design that has been demonstrated to mitigate B_1^+ inhomogeneity, manifest as center brightening, for high-field magnetic resonance imaging (MRI). Parallel transmission achieves spatially-tailored pulses through multiple radiofrequency (RF) excitation coils that can be activated independently. In this work, simulations of magnetic fields in numerical phantoms using an FDTD solver are used to estimate the excitation profiles for an 8-channel RF head coil. Each channel is driven individually in the presence of a dielectric load, and the excitation profiles for all channels are combined post-processing into a B_1^+ profile of the birdcage (BC) mode. The B_1^+ profile is calculated for a dielectric sphere phantom with material properties of white matter at main magnetic field strengths of 3T and 7T to demonstrate center brightening associated with head imaging at high magnetic field strengths. Measurements of a circular ROI centered in the image show more B_1^+ inhomogeneity at 7T than at 3T. The B_1^+ profile is then simulated for a numerical head phantom with spatially segmented tissue compartments at 7T. Comparison of the simulated and *in vivo* B_1^+ profiles at 7T shows agreement in the B_1^+ inhomogeneity. The results provide confidence in numerical simulation as a means to estimate magnetic fields for human imaging. This work will allow further numerical simulations to model the propagation of electric fields within the body, ultimately to provide an estimate of heat deposition in tissue, quantified by the specific absorption rate (SAR), which is a limiting factor of the use of high-field MRI in the clinical setting.

Thesis Supervisor: Elfar Adalsteinsson

Title: Associate Professor of Electrical Engineering and Computer Science
Associate Professor of Harvard-MIT Health Sciences & Technology

Contents

List of Figures

List of Tables

Chapter 1

Introduction

As research in Magnetic Resonance Imaging (MRI) strives for improved signal-to-noise ratio (SNR), MRI scanners operating at higher magnetic field strength are a natural choice since SNR is linearly proportional to the strength of the main magnetic field. Results show that averaged SNR in a 7T scanner is at least 1.6 times larger than that of a 4T scanner and are largely in agreement with theoretical predictions [1].

A critical limitation of human brain imaging at 7T is spatial inhomogeneity of the magnitude of the B_1^+ excitation field—often seen as 'center brightening' in the image—that accompanies standard radiofrequency (RF) coils designed for lower field strengths [2],[3]. Spatial inhomogeneity arises as a consequence of the reduction in relative permittivity of dielectrics in the presence of stronger magnetic fields, coupled with the increase in frequency of the excitation field to maintain the resonance condition. The net result is a decrease in wavelength that accompanies RF excitation at higher magnetic field strengths. In 7T scanners, the RF wavelength is comparable to the size of the head, allowing for interference effects in the center of the head. The extent of spatial inhomogeneity in head imaging at lower field strengths is less significant, but center brightening does exist at lower field strengths, especially in body imaging since the large size of the torso permits interference of longer wavelengths [4].

Center brightening negatively impacts the reconstructed images in two ways: in causing spatially-dependent SNR and contrast. Though the SNR profile can be rectified using proper filtering techniques, there is no known way to recover the correct contrast [4].

One approach to mitigate B_1^+ inhomogeneity with RF pulse design uses tailored excitation profiles in the low-flip angle domain to modulate the B_1^+ excitation field. Slice-selective spoke trajectories from conventional single-channel RF excitation coils, for example, can produce the necessary excitation profile but have long pulse durations because of the number of k_z spokes required and because of limitations on gradient amplitude and slew rate [5].

Parallel transmission (pTx) is a promising improvement to coil design that has been demonstrated to mitigate B_1^+ inhomogeneity. Parallel transmission achieves spatially-tailored pulses through multiple RF excitation coils that can be activated independently [6]-[12]. Compared to single-channel excitation, pTx can create the same excitation using fewer k_z spokes, thus reducing the pulse duration.

Care must be taken when designing RF pulses on multiple excitation channels to avoid excessive constructive interference of the electric fields emitted by the individual coils. Body tissue has electrical conductivity and will heat in the presence of electric fields. The extent of this heating, quantified by the specific absorption rate (SAR), is proportional to the square of the electric field amplitude and to the conductivity of the tissue [6]. Limits on both the local SAR (averaged within any 1g of tissue) and global SAR (averaged over the imaged subject) maintain RF safety for human subjects participating in MRI studies. For clinical operation in the United States, the Food and Drug Administration refers to the limits set by the International Electrotechnical Commission; global head SAR must not surpass 3 W/kg averaged over any 10 minute period while local SAR for head imaging must not surpass 8 W/kg averaged over any 5 minute period [13].

Numerical simulation of pTx coil arrays is a valuable tool to estimate the propagation of electromagnetic waves through tissue and to verify that SAR requirements are being met [14].

Simple geometrical shapes, despite allowing for analytical results, have limited application as anatomical models. SAR levels vary depending on the individual anatomy of the patient, and using numerical simulations is the more practical route towards testing the broad range of anatomical variation between subjects required to ensure safety [14].

An 8-channel parallel transmission head coil has been built and is being tested at the Athinoula A. Martinos Center for Biomedical Imaging in Charleston, MA [4], [9]. The goal of this thesis is to compare the experimental B_1^+ profiles of *in vivo* images with those obtained with the simulation software, Semcad (Schmid & Partner Engineering AG, Zürich, Switzerland). The simulated results will ultimately allow for characterization of the SAR using the 8-channel coil.

Chapter 2

Background

2.1 The Basics of Magnetic Resonance Imaging

Nuclear Magnetic Resonance

Hydrogen atoms have intrinsic nuclear spin angular momentum. When body tissue is in the presence of a strong uniform external magnetic field $\vec{B}_0$, a small fraction of its constituent hydrogen protons will align with the magnetic field, giving rise to a net magnetic moment $\vec{M}$ of magnitude M_0 within the object.

The protons can be excited to a higher energy state by applying a radiofrequency (RF) electromagnetic wave $\vec{B}_1$ perpendicular to the main $\vec{B}_0$ field. This applies a torque to the magnetic dipoles according to the Bloch Equation

$$\frac{d\vec{M}}{dt} = \gamma\vec{M} \times \vec{B} - \frac{M_x\hat{x} + M_y\hat{y}}{T_2} - \frac{(M_z - M_0)\hat{z}}{T_1} \quad \textbf{(Eq. 1)}$$

where γ is the gyromagnetic ratio specific to the nucleus type; and T_1 and T_2 are relaxation parameters of the tissue that describe the rate at which the transverse and longitudinal components of $\vec{M}$ reequilibrate along $\vec{B}_0$. The finite-duration RF pulse ends once the net magnetic moment $\vec{M}$ is in the transverse plane, at which point $\vec{M}$ precesses about $\vec{B}_0$ at a frequency proportional to the strength of the external magnetic field. Specifically, precession occurs at the Larmor frequency w_0, which is given by

$$w_0 = \gamma|\vec{B}_0| \quad \textbf{(Eq. 2)}$$

The precessing spins create a dynamic magnetic flux in the transverse plane that can be detected as an electromotive force (EMF) by one or more conductive loops, called receive coils, according to Faraday's Law.

The process of receiving and encoding the data for image reconstruction is an expansive field. There are several excellent texts that delve into the theory of generating images using MRI [15], [16]. For the purposes of this thesis, limiting the discussion to the RF excitation stage of the MR scan is sufficient.

Magnetic Fields in a Dielectric

A dielectric is a type of material that becomes polarized in the presence of an electric field, quantified by the permittivity ε of the dielectric material. The wavelength of an electromagnetic wave within a dielectric depends on the permittivity of a dielectric since

$$\lambda_{dielectric} \approx \frac{\lambda_{vacuum}}{\sqrt{\varepsilon_r}} = \frac{c}{f\sqrt{\varepsilon_r}} \quad \textbf{(Eq. 3)}$$

where ε_r is the permittivity of the material relative to vacuum, c is the speed of light, and f is the frequency of the wave. Further; different anatomical structures in the body have different permittivity since their unique chemical environments respond uniquely to applied electric fields, as depicted by Figure 1 for white matter, gray matter, and cerebrospinal fluid (CSF). The wavelength of the RF wave in these tissue types is also calculated.

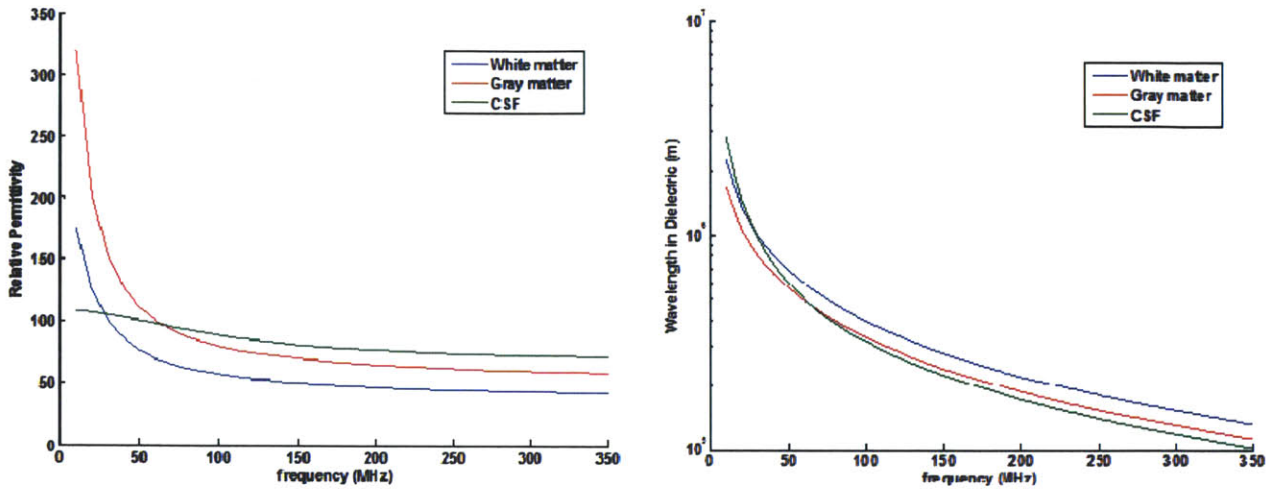

Figure 1 – Relative permittivity ε_r (left) and wavelength λ (right) of different body dielectrics as a function of EM wave frequency.

2.2 The Excitation Field

RF Transmission on a Single Coil

Just as nuclear spins precess at the Larmor frequency once excited into the transverse plane, so is the excitation pulse most effective in rotating the spins when it is applied on resonance with the nuclear spins, that is, at the Larmor frequency. Common MRI scanners used clinically have external B_0 field strengths of 1.5T and 3T, so RF excitation pulses on these scanners are tuned to a frequency of 63.8MHz and 127.6MHz, respectively. Experimental MR scanners operating at 7T have RF coils tuned to 297.3MHz.

The excitation pulse, when coupled with gradient fields $\vec{G}$ that add linear perturbations to the external $\vec{B}_0$magnetic field, will excite a spatially-selective region within the object, called the excitation profile. Typically, the region could be a large 3D slab, thin 2D axial slices, or small 3D volumes as used in spectroscopy, though the excitation profile need not be limited to these

simple geometries [4]. In fact, to mitigate B_1^+ inhomogeneity in 2D slices, excitation profiles are designed to be the inverse of the inhomogeneity [4].

The specific design of the excitation profile is founded on (Eq. 1), though simplifying assumptions are made to achieve a linear equation. First, the pulse duration is assumed to be sufficiently short (between 200μs and 5ms) to render the T_1 and T_2 relaxation terms negligible [16]. Second, the small tip angle approximation for the magnetization vector is made, with the resulting linear equation

$$m_{x,y}(\vec{r}) = i\gamma M_0 \int_0^T B_1(t) e^{i\vec{r}\cdot\vec{k}(t)} dt \qquad \textbf{(Eq. 4)}$$

where

$$\vec{k}(t) = -\gamma \int_t^T \vec{G}(s) ds \qquad \textbf{(Eq. 5)}$$

An important observation is that (Eq. 4) effectively defines the spatial excitation profile as the inverse Fourier Transform of the temporal $\vec{B}_1$excitation pulse envelope. The term $\vec{k}(t)$ thus defines a trajectory in the Fourier space ("excitation k-space"), which depends on the amount of remaining gradient $\vec{G}$ left to be applied during the excitation pulse. It should be noted that the small tip angle approximation is valid for relatively large tip-angles, including 60° and even approaching 90°, though the approximation does fail for 180° pulses [17].

To maximize the effectiveness of the RF pulse in creating the desired excitation profile, the high-energy region of k-space must be covered as thoroughly as possible while satisfying the Nyquist limit,

$$\Delta k \leq \frac{1}{2 \cdot FOV} \qquad \textbf{(Eq. 6)}$$

to avoid aliasing of the excitation profile. Conversely, the duration of the RF pulse must be kept short to avoid detrimental T_1 and T_2 relaxation. With hardware and biological limitations on the

maximum gradient amplitude and slew rate $d\vec{G}/dt$, the design of the trajectory is an important component to achieving the desired excitation profile.

As a simple yet practical example of RF excitation, consider the excitation of a uniform axial slice using a single transmit coil. According to the Fourier relationship of the magnetization profile and the amplitude of the excitation pulse, the $\vec{B}_1$ field should be deposited with a sinc-like distribution in the $k_x k_y$ plane. Further, a thin slice is achieved by depositing the $\vec{B}_1$ field with a large extent in k_z. At low B_0 field strengths, a single coil (and systems of multiple coils driven by the same modulating amplitude but with different, fixed phase shifts, such as quadrature or birdcage coils) is capable of producing a uniform excitation profile, but using this same technique at high B_0 field strengths introduces inhomogeneity into the excitation profile.

The excitation profile of a nonuniform 2D slice, such as one used to mitigate B_1^+ inhomogeneity, follows similar design principles but requires a different distribution of RF deposition in k-space. The mitigation pattern is slowly varying in the plane, thus for a sharp slice profile, the high-energy region of k-space will surround the k_z axis. A spoke trajectory is used to traverse k-space [4], [5], [18].

Acceleration of RF Transmission via Parallel Transmit Coils

The desired excitation profile can be achieved using single transmit coils. However, for the purpose of B_1^+ mitigation, the number of k_z spokes that must be used in order to sufficiently cover k-space requires a long RF pulse. For instance, a sparsely-designed 7.5ms 19 spoke pulse has been shown to achieve sufficient excitation modulation in a 20mm thick slab [5].

Parallel transmission is a strategy to shorten the duration of RF pulses. It relies on systems of *N* multiple coils driven independently with respect to amplitude and phase. Each coil

has a unique sensitivity profile – that is, each coil excites a localized, spatially-varying region of the magnetization slice. Linear independence of the coil sensitivity profiles allows for a reduction of the number of k_z spokes because each spoke contributes excitation information to the N different coils, which can be combined to produce the net excitation profile.

In reality, the coil sensitivity profiles are not orthogonal because they overlap and have rapid spatial variation, so an acceleration of N cannot be achieved. The exact acceleration will depend on the number of coils and the coil geometry, since more transmit coils have more excitation information but also more overlap and spatial variation. Despite this limitation, experiments have shown that 8 spokes on 8-channel pTx coils are enough to achieve the same excitation profile as a 41 spoke pulse on a single transmit coil [10]. Further, novel algorithms show that the number of spokes can be reduced to 4 spokes on 8-channel RF excitation coils [11] and 2 spokes on 16-channel RF coils [12].

The Circularly-Polarized $B_1^{+/-}$ Fields

A single coil generates a linearly-polarized B_1 field, but it must be decomposed into two circularly-polarized fields with opposite polarity in order to excite the magnetization [2]. The $B_1^{\pm}$ fields represent the two circularly-polarized fields and are calculated using:

$$B_1^{\pm} = \frac{1}{2}(B_x \pm iB_y). \qquad \textbf{(Eq. 7)}$$

Only one of the fields precesses in the same direction as the proton magnetic moments and contributes to excitation.

The birdcage (BC) configuration drives multiple coils with the same amplitude modulation in a way that their $B_1^{\pm}$ fields add coherently. The coils are distributed evenly in a

circular pattern around the head and the $B_{1,n}^{\pm}$ fields from the N total coils are then recombined into the BC mode by adding a phase to each coil according to [8]:

$$B_{1,BC}^{\pm} = \frac{1}{\sqrt{N}} \sum_{n=1}^{N} B_{1,n}^{\pm} e^{\mp i(n-1)2\pi/N} \qquad \textbf{(Eq. 8)}$$

The effect that RF wavelength has on B_1^+ homogeneity of the BC mode can be estimated by considering the effect only on white matter. At the magnetic field strengths of 3T and 7T, the wavelength of RF waves within white matter is 32.4cm and 15.2cm, respectively. For an 18cm diameter sphere of white matter, which roughly corresponds to the size and geometry of the head, the individual coil fields will superimpose in phase at the center of the sphere. At 7T, the amplitude of the RF waves is near a maximum at the sphere center, giving rise to a large B_1^+ field amplitude. Conversely, at 3T, the amplitude of the RF waves is less than maximum at the sphere center, giving rise to a large B_1^+ field amplitude; further, the fields are more slowly spatially-varying so the inhomogenity is less localized to the sphere center.

2.3 Field Simulations

Classification of Numerical Solvers

Several algorithms and tools exist that allow for the numerical simulation of electromagnetic fields within the body. Computationally-efficient approximations of Maxwell's Equations, either in the integral or differential form, are used to model the propagation of electromagnetic waves in a system. Solutions can be computed in the frequency domain or in the time domain. Frequency domain analysis, in which time-harmonic behavior is assumed, has the benefit of being more suited to obtaining analytical solutions. Time-domain analyses are

easier to formulate and adapt in computer simulation models without complex mathematics. Additionally, solutions from time-domain analyses can cover a wide frequency range with a single simulation run, which is useful for broadband excitation.

Within each category of solver exist several algorithms that have different merits depending on the system to be modeled. The boundary element method (BEM) – also called the method of moments (MoM) – is a popular integral equation solver that uses Green's functions. Because it works with boundaries rather than full volumes, BEM is computationally efficient for problems with a small surface to volume ratio. However, the matrix solutions resulting from BEM formulations are fully populated, which is taxing on the computation time and memory requirements for large domains.

Some numerical solvers, such as the Finite Element Method (FEM) can be used with either form of Maxwell's Equations. FEM is particularly useful when the desired precision varies over the entire domain. The solution matrices in FEM are banded because of near-neighbor node coupling, thus less memory is required than BEM.

The Finite Difference Method (FDM) simplifies the differential form of Maxwell's Equations into finite difference equations meeting appropriate boundary conditions. The finite-difference time domain (FDTD) algorithm used in this work simulates the electromagnetic fields based on a time domain FDM algorithm. The FDTD begins with a discretized model of the body and coil circuitry then estimates a linear solution to Maxwell's equations for each voxel, iterating the process over small time steps. FDTD has been widely implemented in many software packages, such as Remcom and Semcad, which allow for the integration of model design and field simulations.

Complications in Numerical Simulations

There are several complicating factors in the design of numerical simulations. Memory limitations are commonly encountered, limiting the resolution and geometrical complexity of the model.

Even with sufficient memory, the duration of simulations can also be prohibitive for large models. In order to maintain the linearity of the finite difference equations, the numerical integrator must use small time steps with a maximum value limited by

$$\Delta t \leq \frac{\Delta x}{c\sqrt{3}} \qquad \textbf{(Eq. 9)}$$

where c is the speed of light and $\sqrt{3}$ appears because the simulation space is 3-dimensional [19]. Thus, for a resolution of 2mm, a time step smaller than 3.85ps must be used.

The FDTD simulation of electromagnetic waves can be accelerated by the parallel computation of field solutions on graphical processing units (GPUs). Adaptive gridding is another approach to decreasing both simulation duration and memory. Adaptive gridding uses a nonuniform discretization with a fine resolution near important model elements and a coarse resolution in unpopulated regions of the simulation space.

The quality and stability of the numerical simulations is affected by more than the time step of the integrator. Discretizing the model is a potential source of error. Model elements with thin dimensions, such as a wire or thin metallic sheet, may be entirely eliminated during the discretization process; model elements with non-Cartesian geometry or alignment can become distorted. For example, a thin rectangular sheet might be discretized as a diagonal chain of squares adjoined corner to corner, which would change the path of an electrical current applied to the sheet. Finally, to ensure stability, the absorbing boundary of the simulation space must be placed far enough from the model so that the RF waves are not reflected.

Chapter 3

Model

3.1 Software Requirements

The primary software package used in simulations is Semcad X running on a Windows 64 bit operating system. Simulation acceleration is performed on a Tesla C1060 card (NVIDIA; Santa Clara, CA) using NVIDIA Cuda drivers and Toyama (AXWare; Austin, TX) libraries.

3.2 Eight-channel transmission coil

An 8-channel coil model with RF shield has been imported into Semcad. Each channel consists of 16 individual coil elements made of thin perfect electrical conducting (PEC) sheets, as shown in Figure 3. The twelve vertical PEC elements have 1.8cm height and 3mm width; the four horizontal elements have 2.1cm width and 3mm height. The individual coil elements are separated by 3mm so that each coil has overall dimensions 13.5cm total length and 4.5cm total width. The RF shield is thin PEC, 40cm in diameter and 33cm in height, and is concentric with the 8 coils.

The coil elements are joined by identical tuning capacitors and PEC wire. At the bottom of the coil is a port consisting of a harmonic voltage source with 50Ω internal resistance and tuning and matching capacitors, shown in Figure 2. A PEC wire is added to the port so that the elements are aligned on a rectilinear grid. The capacitors of the coils in the anterior/posterior direction have identical values, as do the capacitors of the coils in the left/right direction and the

capacitors that are slanted with respect to the FDTD grid, though the capacitor values of these three orientations are independent.

3.3 Dielectric Loads

The magnetic fields have been simulated for the 8-channel coil with a dielectric spherical load and with a 2mm isotropic resolution Virtual Family Ella body phantom provided by Semcad (shown in Figure 4). The dielectric sphere has a diameter of 18cm and is centered in the coil. The dielectric sphere has also been simulated at the frequencies 128MHz and 297MHz corresponding to the common clinical external magnetic field strengths of 3T, and 7T. The material properties of white matter were used, with conductivity σ, relative permittivity $\varepsilon/\varepsilon_0$, and wavelength λ within the dielectric as described in the following table [20]:

Table 1 – Dielectric properties of white matter at the two simulated field strengths of 3T and 7T

ω [MHz]	B_0 [T]	σ [S/m]	$\varepsilon/\varepsilon_0$	λ [m]
128	3.0	0.342	52.6	0.324
297	7.0	0.412	43.8	0.152

The tissue density, permittivity, and conductivity for each tissue type of the Ella phantom are calculated within Semcad for the frequency of 297MHz. The background of the simulation volume is air.

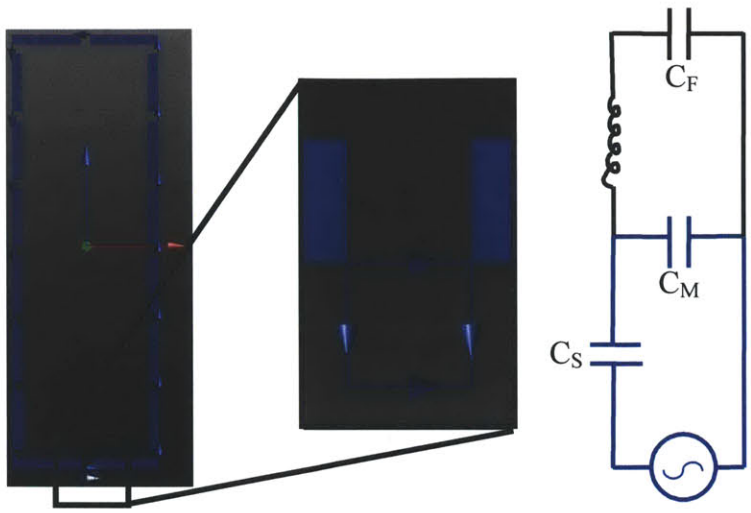

Figure 2 - Model of a single coil of the 8-channel RF excitation head coil (left) and close-up of port (center). A schematic of the coil is also shown (right), with the port highlighted in blue. The rest of the coil is condensed into the equivalent circuit represented in black by C_F and the inductor.

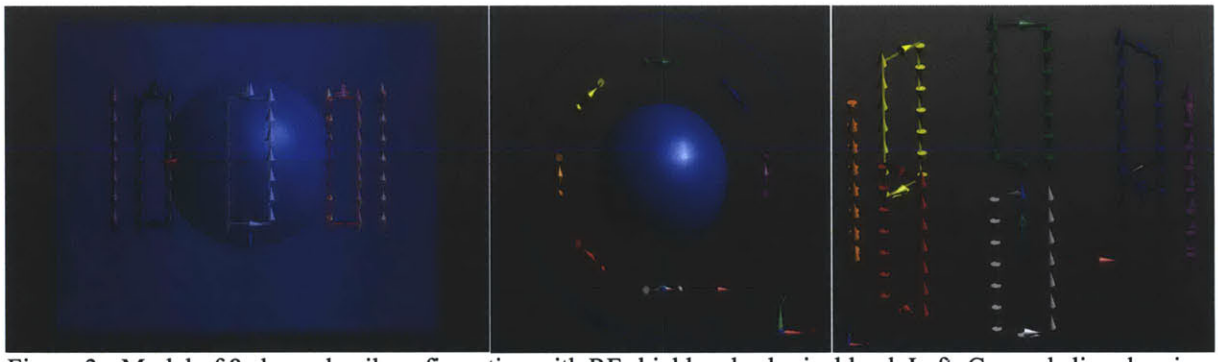

Figure 3 - Model of 8 channel coil configuration with RF shield and spherical load. Left: Coronal slice showing geometry of coils, dielectric sphere, and RF shield. Height of RF shield is 33cm. Center: Axial slice of model. Right: Off-axis view of coil geometry (RF shield and spherical load are hidden).

Figure 4 – The 2mm resolution Virtual Family model of Ella in the 8-channel coil with RF shield. Left: Coronal slice of model. Right: Axial slice of model.

3.4 Excitation

All simulations run the voltage source at 1V peak voltage for 100 periods, with a ramp on during the first period. The simulations use an FDTD solver to iterate through time steps. Only a single coil is excited during each simulation. The voltage source of unexcited coils is disregarded during the simulation so that the ports appear open. Field estimates for a birdcage configuration were calculated in MATLAB (MathWorks; Natick, MA) by recombining the individual coil solutions.

The boundary of the modeling space is perfectly absorbing. A minimum of 10 voxels pad the outside of the RF shield inside the boundary to prevent ringing artifacts caused by reflections.

3.5 Discretization and Image Resolution

The dielectric sphere and Ella are simulated at a resolution of 2mm. Despite this, the gridding algorithm aligns the baselines with natural object boundaries in the model, so the grid deviates up to 10% from isotropic resolution. Further, the solver changes the local wavelength of the fields to reflect changes in permittivity and conductivity, so to keep the grid as uniform as possible, the boundaries of dielectric materials are ignored and only the PEC elements are considered when designing the grid. The resulting simulated fields are regridded in MATLAB onto a $(2\text{mm})^3$ isotropic grid.

The simulation of Ella takes 40 minutes per coil for a total simulation time of 5 hours and 20 minutes. Stability of the FDTD method requires proportionality between the spatial resolution and the iterative time step so doubling the resolution in each dimension would undesirably increase the simulation duration by a factor of 8 [19].

Chapter 4

Methods

4.1 Tuning

Before running a simulation, each coil must be tuned to the Larmor frequency. Considering each coil as a simplified circuit shown in Figure 2, tuning is done by adjusting the capacitance C_F following

$$f = \frac{1}{2\pi\sqrt{LC}} \Rightarrow \frac{{f_0}^2}{{f_1}^2} = \frac{C_0}{C_1} = \frac{\frac{15}{C_{F,1}} + \frac{1}{C_M}}{\frac{15}{C_{F,0}} + \frac{1}{C_M}} \quad \textbf{(Eq. 10)}$$

where the subscript 0 indicates the desired capacitances at the Larmor frequency f_0 and the subscript 1 indicates the current capacitances at untuned frequency f_1. The frequency of the unturned coil is estimated by the reflection coefficient S_{11}, which physically represents the ratio of the reflected voltage to the driving voltage at a port [19]. The minimum of S_{11} over a broad frequency band occurs at the resonant frequency of the system.

Although all eight coils must be tuned, recalling that there are only three unique coil types (the anterior/posterior coils, the left/right coils, and the four coils slanted with respect to the FDTD grid) reduces the degrees of freedom. The reflection coefficient S_{11} is calculated for each coil type and used to provide an estimate of the needed capacitances C_F to achieve resonance at the Larmor frequency. However, coupling of the coils makes this estimate imperfect, so tuning is performed iteratively until all coils are tuned to within an acceptable range of the Larmor frequency.

In real MR scanners, the coils are also matched so that their reflection coefficient at the resonant frequency is as small as possible. This can similarly be implemented in the numerical model by adjusting the capacitances C_M and C_S but it will affect the frequency to which the coil is tuned. Thus, to completely tune and match the system requires the interleaving of separate tuning and matching iterations for all coil types, which introduces an additional level of complexity. Due to time constraints, only tuning was performed on the coils for the work in this thesis.

4.2 Quantification Metrics

The presence of B_1^+ inhomogeneity is easily qualifiable by visual inspection of the center brightening present in acquired MR images. Quantifying the extent of B_1^+ inhomogeneity is a more challenging task with a host of possible metrics; this work is based on metrics used previously in the context of B_1^+ inhomogeneity quantification for parallel RF excitation coils, [9], [12]. The analysis will only be performed on a region of interest (ROI) surrounding the center brightening artifact to reduce the effect of spatially-varying fields near the outside edge of the imaged object caused by the individual coil excitation profiles.

First, the intensity of the ROI is normalized to 1 and the mean μ and standard deviation σ of the normalized ROI are calculated. Normalization is useful because the coils in each simulation and experiment are tuned and matched differently so the comparison should not consider differences due to absolute field magnitude. Next, the root magnitude mean-squared error (RMMSE) is calculated according to

$$RMMSE = \sqrt{\frac{\sum_{ROI}(|I_i| - \mu)^2}{\sum_{ROI} 1}} \qquad \textbf{(Eq. 11)}$$

for each pixel in the ROI, where I_i is the normalized intensity at pixel i within the ROI. The last metrics are <10%dev and <20%dev which give the percentage of pixels in the ROI that have intensity within 10% or 20% of the mean intensity.

Chapter 5

Results

5.1 Dielectric sphere at 3T and 7T

The electromagnetic fields have been simulated for a spherical load in the 8 channel coil array with RF shield. The magnitude B_x, B_y, and B_z fields for a single excited coil and for the birdcage configuration are shown in Figure 5. Even though only a single coil is excited in the top row of images, coupling to other coils is visible. These images follow the radiological convention, in which x increases in the right-left (RL) direction, y increases in the posterior-anterior direction, and z increases in the superior-inferior direction.

The $B_1^{+/-}$ fields for an individual coil are calculated in MATLAB using (Eq. 7). The coils are then recombined into a birdcage configuration (BC) by adding a phase to each coil with the result shown in Figure 6. The presence of the load is not easily visible on a linear display scale but when a mask is applied to the external fields, the fields in the dielectric become more apparent, as shown in Figure 7 for the dielectric sphere in birdcage configuration.

The $B_1^{+/-}$ fields exhibit a larger degree of center brightening as the external field strength increases, consistent with experiment results [9]. The wrapped phase maps are smooth throughout the models, as expected from slow spatially-varying fields. The ROI used for quantitative analysis is the inner circle of the phantom with radius 4.5cm—half that of the phantom itself. The ROI is the region within the black rings in the Figure 7 $|B_1^+|$ images.

The measurements summarized in Table 2 are consistent with the observation that the $|B_1^+|$ fields in the center of the sphere are larger at 7T than at 3T. The mean $|B_1^+|$ of the sphere at

7T is substantially smaller than at 3T while the standard deviation is four times larger at 7T than at 3T. These two measurements show the extent that the $|B_1^+|$ field diminishes outside the center peak. Almost all pixels of the 3T ROI but only one-third of the pixels in the 7T ROI are within 10% of the mean intensity. Even 20% of the pixels in the 7T ROI deviate from the mean by more than 20% of the mean. Interestingly, the RMMSE at both external field strengths is equal to the standard deviation σ, indicating that the estimator is unbiased.

Table 2 – Metrics comparing spherical dielectric ROIs at 3T and 7T

	μ	σ	RMMSE	<10%dev [%]	<20%dev [%]
3T	0.931	0.030	0.030	99.8	100
7T	0.760	0.129	0.129	35.1	80.0

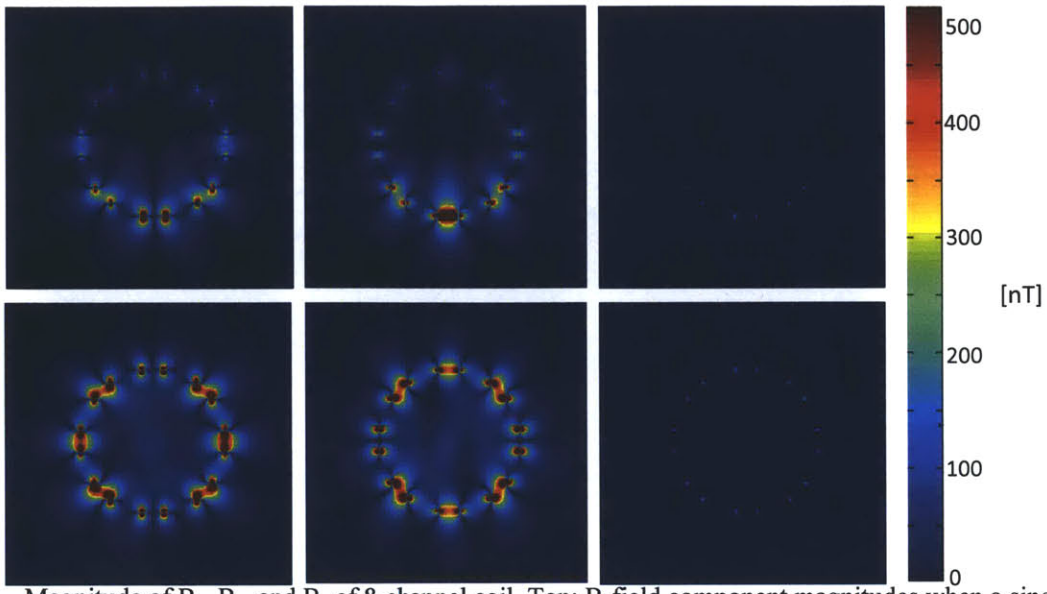

Figure 5 – Magnitude of B_x, B_y, and B_z of 8-channel coil. Top: B-field component magnitudes when a single coil is excited. Bottom: B-field component magnitudes when all 8 coils are combined in a birdcage configuration. The load is a dielectric sphere and the image is an axial slice through the center of the sphere.

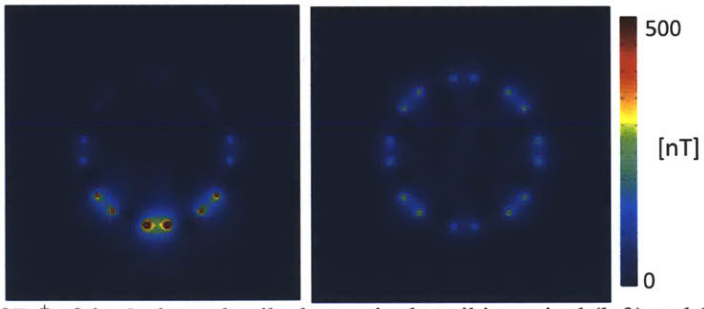

Figure 6 – Magnitude of B_1^+ of the 8-channel coil when a single coil is excited (left) and for all eight coils combined in a birdcage configuration (right). The load is a dielectric sphere and the image is an axial slice through the center of the sphere.

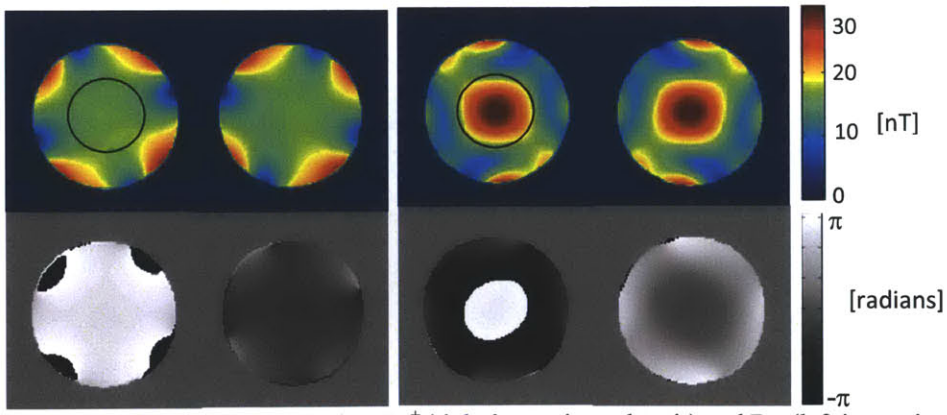

Figure 7 – Magnitude (top) and phase (bottom) of B_1^+ (right image in each pair) and B_1^- (left image in each pair) for 8-channel coil with 18cm-diameter spherical load, birdcage excitation (axial view). The left set of images are for $\omega = 128$MHz ($B_0 = 3$T, $\lambda = 32.4$cm); the right set of images are for $\omega = 297$MHz ($B_0 = 7$T, $\lambda = 15.2$cm). The black ring indicates the ROI used for evaluation. The magnetic field of the background has been masked to generate the images. The driving voltage is 1V.

5.2 Numerical Head Phantom at 7T

Central brightening is also visible in the magnitude $B_1^{+/-}$ fields with the Ella phantom, shown in Figure 8 and Figure 9. The wrapped phase maps in Figure 9 are smooth throughout the models, as expected. Analysis of the numerical phantom is postponed to the next section.

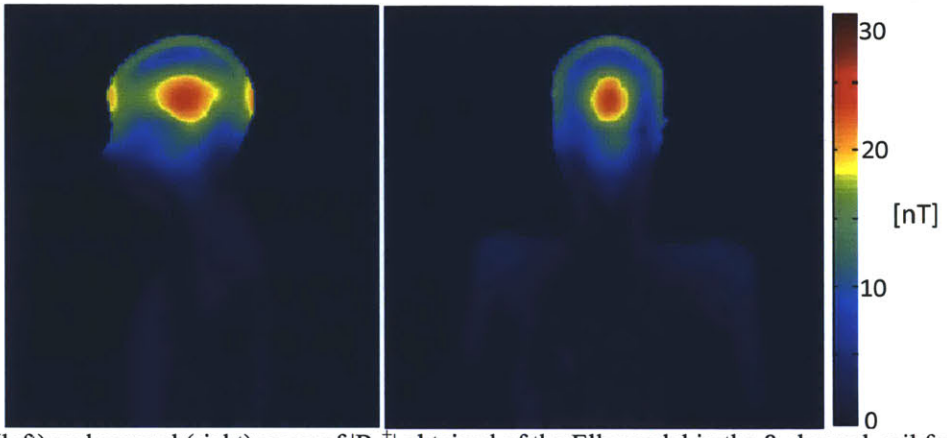

Figure 8 – Sagittal (left) and coronal (right) maps of $|B_1^+|$ obtained of the Ella model in the 8-channel coil from birdcage excitation.

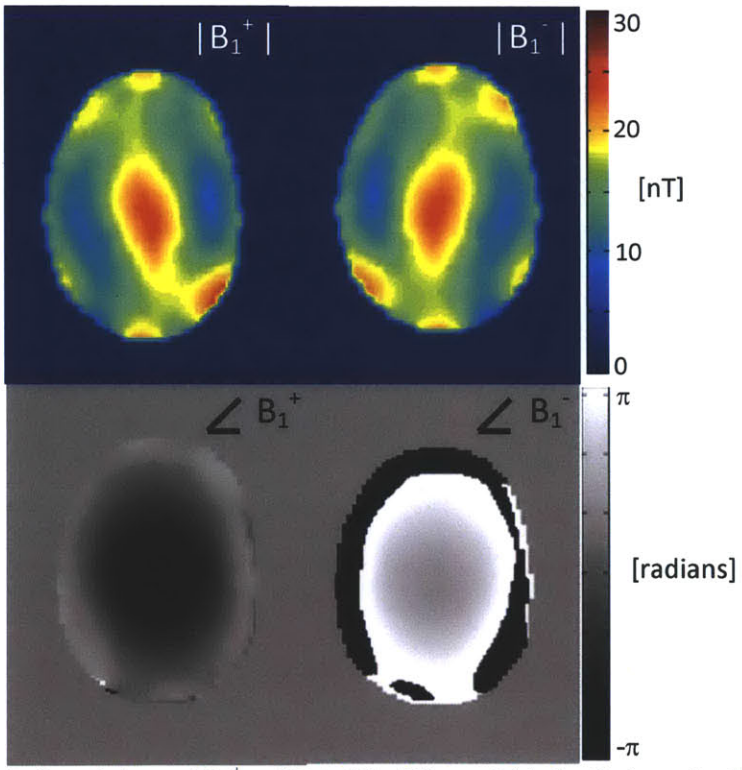

Figure 9 – Axial view of the magnitude and phase of B_1^+ and B_1^- of the Ella model in the 8-channel coil with birdcage excitation. The simulations are run on a nonuniform grid of maximum resolution 2mm and the results are remapped onto a uniform $(2mm)^3$ grid. The slice shown is at the maximum of the $|B_1^+|$ field shown in Figure 8.

5.3 B_1^+ of Simulated Head Model versus in vivo scan at 7T

The magnitudes of the central brightening in the Ella simulation and in the *in vivo* sample are in good agreement, shown in the ROIs of Figure 10 and in the $|B_1^+|$ profile in a left-right cross-section through the center of the images depicted in Figure 11. Discrepancy in the size of the head should not be worrisome as only one slice of *in vivo* data was acquired (at the bore of the magnet); the discrepancy is a result both of imaging/simulating both different head sizes and different slices within the head.

Quantitative metrics summarized in Table 3 are consistent with the observation that the B_1^+ fields *in vivo* and in the numerical phantom are in agreement, though there are some subtle differences. Although the normalized $|B_1^+|$ field in the *in vivo* and numerical phantom ROIs have the same mean value, the standard deviation of the numerical phantom is 2-3 times larger than that of the *in vivo* ROI, indicating that the $|B_1^+|$ field in the numerical phantom has a larger plateau of intense voxels and a sharper drop-off of field intensity outside the centrally-bright plateau. Correspondingly, the <10%dev and <20%dev of the *in vivo* ROI is between 75% and 90%, less than the near 100% <10%dev of the phantom ROI.

Table 3 — Metrics comparing *in vivo* ROI to numerical phantom ROI at 7T

	μ	σ	RMMSE	<10%dev	<20%dev
in vivo	0.900	0.0265	0.0662	78.3	87.0
phantom	0.899	0.0702	0.0729	99.3	99.5

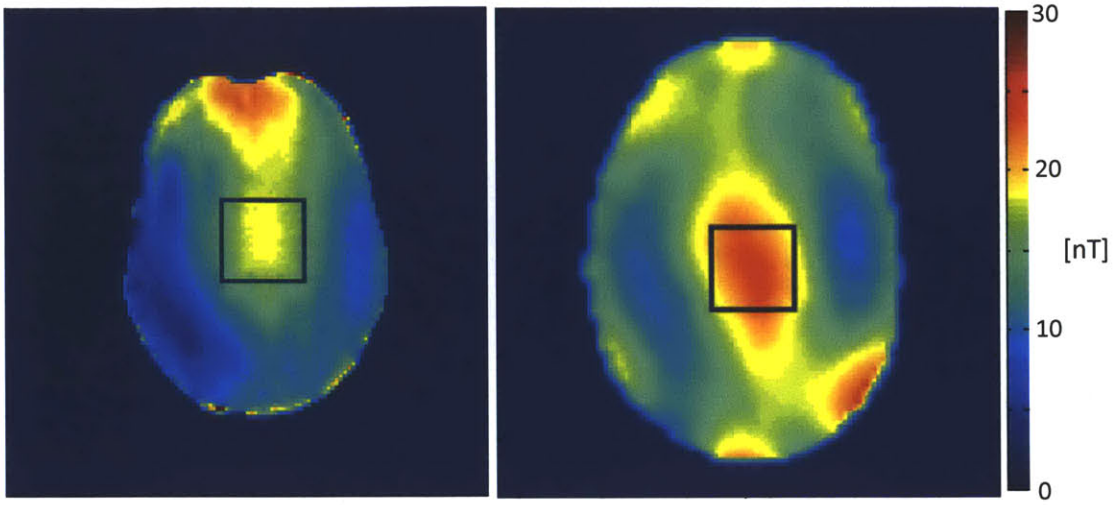

Figure 10 – $|B_1^+|$ of an in vivo sample (left) compared to the Ella model (right), both in an 8-channel coil with birdcage excitation. Both ROIs are $(4\text{ cm})^2$ centered on the central bright peak in the brain; the FOV of each image is $(24\text{ cm})^2$.

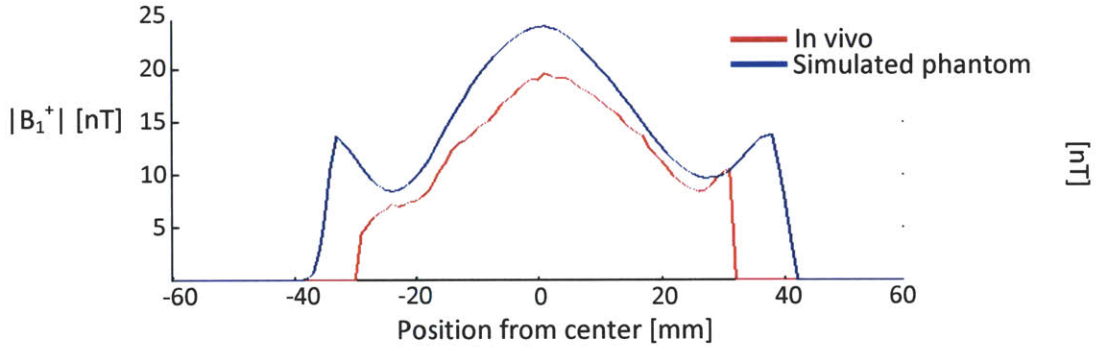

Figure 11 – $|B_1^+|$ of an *in vivo* sample (blue) compared to the numerically simulated Ella model (red) in a LR cross-section through the center of each ROI.

Chapter 6

Discussion

An 8-channel parallel RF excitation coil has been modeled in Semcad following the design of a head coil built for 3T and 7T MRI scanners. RF excitation fields played individually on each coil were combined into a birdcage mode to yield magnitude and phase B_1^+ profiles. Simulations were run for an 18cm diameter dielectric sphere with properties of white matter at 3T and 7T and for a numerical head phantom at 7T.

Insignificant B_1^+ inhomogeneity at 3T was measured in an intensity-normalized ROI in the dielectric sphere. B_1^+ inhomogeneity manifest as a center brightening artifact was present in both the dielectric sphere and numerical head phantom profiles at 7T. Interestingly, the normalized sphere ROI had a mean of 0.76, a standard deviation of 0.13, and both <10%dev and <20%dev well under 100%, whereas the numerical head phantom had a larger mean of 0.9, a smaller standard deviation of 0.07, and a <%10dev of approximately 100%. In total, these measurements indicate a more inhomogeneous B_1^+ profile for the dielectric sphere than for the head phantom. Part of this finding can be explained by the different size and geometry of the ROIs for the sphere and the head phantom, but experimental results have also shown more B_1^+ inhomogeneity for uniform objects than for homogenous objects like the head [12].

The simulated B_1^+ profile of the numerical head phantom was compared to the B_1^+ profile of a single *in vivo* slice acquired by an 8-channel transmission coil in a 7T MR scanner. The normalized ROIs agree in mean and RMMSE, though the standard deviation in the *in vivo* ROI is more than half that of the phantom ROI, indicating that the center brightening *in vivo* is less sharply localized than in the numerical phantom.

Agreement of the experimental B_1^+ profile and that obtained through numerical simulation give us confidence in simulation as a means to estimate magnetic fields from parallel transmit coils for human imaging. Numerical simulation can be implemented in several phases of parallel transmit coil design and evaluation, ranging from optimization of the number and geometry of RF coils for B_1^+ inhomogeneity mitigation to estimation of local and global SAR.

One limiting factor of this work is the duration of the FDTD simulations. A single iteration of coil tuning took upwards of four hours for the three coil types; three or four tuning iterations were performed for a total simulation time of nearly a day. This duration is prohibitive for the design of RF excitation coils with more than eight channels, and introducing matching would be infeasible for any parallel excitation coil design. In comparison, tuning and matching experimental RF coils involves only the manual dialing of variable capacitors and can be completed in minutes.

One possible remedy is to use other categories of numerical solvers to estimate the B_1^+ profiles. The boundary element method has been proposed as an alternative approach with substantially faster execution time but the numerical phantoms present in BEM software packages are less complex than the Semcad Virtual Family and might not estimate SAR with the same degree of accuracy as would a lengthier simulation in Semcad.

Another current limitation of this work is how it calculates the B_1^+ profile of coils in a birdcage mode from individual coil fields. In principle, the fields of individual coils should be independent and thus can be linearly combined post-processing to derive the birdcage mode B_1^+ profile as was done in this work, but the simulated magnetic fields of a single coil as shown in Figure 5 and Figure 6 demonstrate coupling between the coils. Inter-coil coupling will affect the

generated RF pulse when all coils are excited simultaneously. It would be interesting to see how the birdcage B_1^+ profile changes for a simulation in which all coils are excited simulateously.

Similarly, this work only demonstrates the source of B_1^+ inhomogeneity but does not try mitigation using the inverse field. It would be useful to calculate the other modes (in addition to the birdcage mode) that are combined for ideal B_1^+ mitigation [8]. Implementing the corresponding RF pulse sequence on the eight channels designed to mitigate B_1^+ inhomogeneity would be a fruitful next step for numerical simulation.

With the numerical phantom implemented in Semcad, another future direction would be estimation of local and global SAR. Even though SAR cannot be measured directly by experimental transmission or receive coils, SAR can be estimated experimentally with MR-compatible electric field probes, however, such hardware is expensive and the results would likely require validation through simulation. Estimating SAR through numerical simulations requires only minimal work because the electric fields are solved concurrently with the magnetic fields and the numerical phantoms include information on tissue conductivity and density. In fact, the Semcad software package includes a tool for directly calculating the temperature of tissue in RF fields that could be investigated as an alternative or additional measure of safety.

References

[1] Vaughan JT, Garwood M, Collins CM, Liu W, DelaBarra L, Adriany G, Anderson P, Merkle H, Goebel R, Smith MB, Ugurbil K. 7T vs. 4T: RF power, homogeneity, and signal-to-noise comparison in head images. Magn Reson Med 2001; 46:24–30.

[2] Ibrahim T, Hue YK, Tang L. Understanding and manipulating the RF fields at high field MRI. NMR Biomed 2009; 22:927–936.

[3] Collins C, Li S, Smith MB. SAR and B_1 field distributions in a heterogeneous human head model within a birdcage coil. Magn Reson Med 1998; 40:847–856.

[4] Setsompop K, Wald LL, Alagapan V, Gagoski B, Hebrank F, Fontius U, Schmitt F, Adalsteinsson E. Parallel RF transmission with eight channels at 3 Tesla. Magn Reson Med 2006; 56:1163-1171.

[5] Zelinski A, Wald LL, Setsompop K, Alagappan V, Gagoski B, Goyal V, Adalsteinsson E. Fast slice-selective radio-frequency excitation pulses for mitigating B_1^+ inhomogeneity in the human brain at 7 Tesla. Magn Reson Med 2008; 59:1355–1364.

[6] Zhu Y. Parallel excitation with an array of transmit coils. Magn Reson Med 2004; 51:775–784.

[7] Grissom W, Yip CY, Zhang Z, Stenger VA, Fessler J, Noll D. Spatial domain method for the design of RF pulses in multicoil parallel excitation. Magn Reson Med 2006; 56:620-629.

[8] Alagappan V, Nistler J, Adalsteinsson E, Setsompop K, Fontius U, Zelinski A, Vester M, Wiggins G, Hebrank F, Renz W, Schmitt F, Wald LL. Degenerate mode band-pass birdcage coil for accelerated parallel excitation. Magn Reson Med 2007; 57:1148–1158.

[9] Setsompop K, Wald LL, Alagappan V, Gagoski B, Adalsteinsson E. Magnitude least squares optimization for parallel radio frequency excitation design demonstrated at 7 Tesla with eight channels. Magn Reson Med 2008; 59:908-915.

[10] Setsompop K. Design algorithms for parallel transmission in magnetic resonance imaging. PhD thesis: MIT, 2008.

[11] Alagappan V. RF coil technology for parallel excitation and reception in high field MRI. PhD thesis: Tufts University, 2009.

[12] Setsompop K, Alagappan V, Gagoski B, Witzel T, Polimeni J, Potthast A, Hebrank F, Fontius U, Schmitt F, Wald LL, Adalsteinsson E. Slice-selective RF pulses for in vivo B_1 inhomogeneity mitigation at 7 Tesla using parallel RF excitation with a 16-element coil. Magn Reson Med 2008; 60:1422–1432.

[13] Center for Devices and Radiologic Health. Guidance for the submission of pre-market notifications for magnetic resonance diagnostic devices. Food and Drug Administration, 1998.

[14] Collins C. Numerical field calculations considering the human subject for engineering and safety assurance in MRI. NMR Biomed. 2009; 22: 919–926.

[15] Nishimura D. Principles of Magnetic Resonance Imaging. Stanford University: Self-published; 1996.

[16] Bernstein MA, King KF, Zhou XJ. Handbook of MRI Pulse Sequences. Elsevier Academic Press; 2004. (pg 67).

[17] Pauly JM, Nishimura D, Macovski A. A k-space analysis of small-tip-angle excitation. J Magn Reson vol. 81, pp 43-56, 1989.
[18] Zelinski A, Wald LL, Goyal V, Adalsteinsson E. Sparsity-enforced slice-selective MRI RF excitation pulse design. IEEE Trans Med Imag 2008; vol. 27, no. 9:1213-1229.
[19] Elsherbeni A., Demir V. The Finite-Difference Time Domain Method for Electromagnetics with MATLAB Simulations. Raleigh, NC: SciTech Publishing Inc; 2009. pg 36.
[20] Gabriel, C., Gabriel, S. Compilation of the dielectric properties of body tissues at RF and microwave frequencies. AL/OE-TR-1996–0037, 1996. <http://niremf.ifac.it/tissprop>